

# Surface Chemistry of Nanometer-Sized Aerosol Particles: Reactions of Molecular Oxygen with 30 nm Soot Particles as a Function of Oxygen Partial Pressure

Amanda M. Nienow,<sup>†</sup> Jeffrey T. Roberts,<sup>\*,†</sup> and Michael R. Zachariah<sup>‡</sup>

Department of Chemistry, University of Minnesota, Minneapolis, Minnesota 55455, and Department of Mechanical Engineering, University of Maryland, College Park, Maryland 20742

Received: October 7, 2004; In Final Form: January 31, 2005

The kinetics of the reaction between soot nanoparticles and molecular oxygen were studied by tandem differential mobility analysis (TDMA). The particles were extracted from the tip of an ethene diffusion flame. Reactions were studied at atmospheric pressure in mixtures of nitrogen and oxygen. The studies involved particles of an initial mobility diameter of 30 nm over broad ranges of temperature (500–1100 °C) and oxygen volume fraction (0–1). Measurements as a function of oxygen partial pressure establish that the oxidation kinetics are not first-order in oxygen volume fraction ( $F_{O_2}$ ). Rather, the oxidation rate increases rapidly and linearly with  $F_{O_2}$  between 0 and 0.05 and then more slowly but still linearly between 0.05 and 1. Temperature dependent measurements are consistent with a reaction pathway involving two kinetically distinguishable oxidation sites which interconvert thermally and through oxidation. Results and conclusions are compared to those of earlier studies on the oxidation of soot.

## Introduction

The atmosphere abounds in all types of aerosol particles, both natural and anthropogenic, including combustion particles (e.g., soot), mineral dust, sea salt, organic particles, and aqueous inorganic acids.<sup>1</sup> Among the most important anthropogenic particles are soot particles.<sup>2</sup> In some urban areas, ~15% of all atmospheric particles between the sizes of 1 and 1000 nm in diameter are soot.<sup>1</sup> Soot consists mostly of elemental carbon, but depending on the combustion source, small amounts of sulfates, nitrates, and metals may also be present. Additionally, often there is volatile organic material adsorbed to the elemental carbon.<sup>3</sup>

The United States EPA has proposed more stringent particulate emission standards to be put into effect in 2007. To meet these standards, a great amount of research is currently devoted to reducing particulate emissions. One proposed method is to oxidize the particles as a means to remove them from the exhaust stream.<sup>4</sup> However, the fundamentals of the oxidation process of nanometer sized soot particles at relevant temperatures and oxygen partial pressures is not fully understood.

Oxidation of soot and soot surrogates has been studied extensively in the past using a variety of techniques.<sup>5</sup> Carbon filaments,<sup>6,7</sup> carbon or graphite rods,<sup>8,9</sup> graphite,<sup>10–12</sup> char,<sup>13</sup> and carbon blacks<sup>14–16</sup> have been used as soot surrogates. Most previous studies on soot generated in flames and/or diesel engines have relied on collecting and/or immobilizing the soot<sup>14,17,18</sup> or on light scattering within a flame environment.<sup>19–21</sup> The majority of previous studies have considered how oxidation depends on temperature. Some work has been published on the order of the oxidation reaction with respect to oxygen partial pressure.<sup>10,15,16,22–24</sup> Most of these studies were conducted at temperatures above 1500 °C, at which temperatures the kinetics

gradually shift from reaction- to diffusion-limited.<sup>24</sup> These temperatures are much higher than temperatures particles would encounter in typical exhaust after-treatments.

We recently described a method to study the kinetics of soot oxidation using on-line aerosol techniques applied to freshly generated, size-selected soot nanoparticles.<sup>2,25</sup> Both ethene and diesel soot have been studied. Kinetics were studied by tandem differential mobility analysis (T-DMA), in which the reaction rate is correlated with reaction-induced changes in particle size. Our method overcomes several of the disadvantages of previous studies. Because the soot is freshly generated and studied by aerosol techniques, effects of aerosol aging and transport are minimized. In addition, a stream of aerosol particles is relatively easily controlled. Last, particle size selection allows size-dependent effects to be examined.

In this paper, we extend our earlier work, which concerned soot oxidation in dry air at atmospheric pressure, to consider the effects of oxygen partial pressure in mixtures of  $O_2$  and  $N_2$ . The total pressure was maintained at 1 atm, with the oxygen partial pressure varied between 0.0 and 1.0 atm. We build further on our earlier work by emphasizing smaller particles than before, of initial mobility diameter of 30 nm. Particles of these dimensions are nearly spherical, in contrast to the more complex aggregate structures of larger particles.<sup>5</sup> This is important because it simplifies the kinetic analysis.

## Experimental Section

The kinetics of soot oxidation were studied by tandem differential mobility analysis (T-DMA) using an atmospheric pressure aerosol flow tube reactor. The aerosol flow reactor, shown schematically in Figure 1, was a modified version of a reactor described in detail elsewhere.<sup>2,25</sup> Briefly, soot particles were extracted into the reactor from the tip of an ethene diffusion flame through a small orifice in a stainless steel tube. The resulting particle stream was swept by an atmospheric pressure carrier gas through a bipolar diffusion charger, which established

\* To whom correspondence should be addressed. Telephone: (612) 625-2363. Fax: (612) 626-7541. E-mail: roberts@chem.umn.edu.

<sup>†</sup> University of Minnesota.

<sup>‡</sup> University of Maryland.

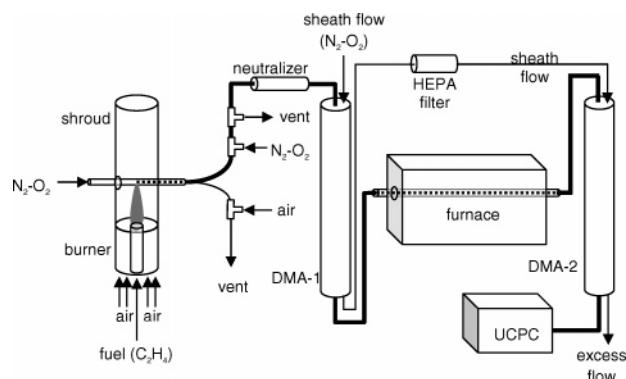


**Figure 1.** Schematic diagram of the experimental apparatus. The bold line indicates the path taken by the soot particles.

a known charge distribution on the aerosol.<sup>26,27</sup> Under the conditions of this experiment, very few (<10%) of all particles had a charge exceeding +1 or -1. Particles were then passed through a differential mobility analyzer (DMA-1, TSI Model No. 3081), which was set to transmit particles of a selected electric mobility. The resulting stream of particles then passed through the reaction zone, a quartz tube encased in a tube furnace. The temperature of the furnace could be set to any value between room temperature (23–26 °C) and 1100 °C. As will be shown below, oxidative and nonoxidative processing took place in the reaction zone which led to changes in particle size. The particle stream was therefore sent through a second DMA (DMA-2, TSI model no. 3085) for mobility and size reclassification, and finally into an ultrafine condensation particle counter (UCPC, TSI model no. 3025A) for detection. The most important difference between this apparatus and that described previously<sup>2,25</sup> is that DMA-2 and the condensation particle counter were replaced by newer models which allowed the investigation and detection of particles as small as 3 nm in mobility diameter.

In any given experiment, the same gas, either dry air, nitrogen, or a synthetic nitrogen–oxygen mixture, was used as both carrier and sheath gas. Compressed air was supplied in-house, and gaseous nitrogen was obtained from liquid nitrogen tanks (99.998% pure with less than 8 ppm O<sub>2</sub>). Compressed air was filtered and dried before use with a series of particulate and coalescing filters and a desiccant drier. The desiccant was changed regularly. Mixtures of nitrogen and oxygen were prepared by simultaneously introducing nitrogen and oxygen (Industrial Grade, 99.5% pure) into a copper mixing coil through calibrated rotameters. The volume percent of oxygen in a mixture ( $F_{O_2}$ ) was taken as

$$F_{O_2} = \frac{f_{O_2}}{f_{O_2} + f_{N_2}} \quad (1)$$

where  $f_{O_2}$  and  $f_{N_2}$  are the oxygen and nitrogen gas flow rates, respectively, as measured by the rotameters. For gas mixtures containing up to 12.5% oxygen by volume, the mixtures were prepared by combining a flow of 35 L per minute (lpm) nitrogen with between 0 and 5 lpm oxygen. Mixtures that were more concentrated in oxygen were prepared using lower values of  $f_{N_2}$ .

Profiles of the gas temperature in the quartz tube reactor were measured with a K-type thermocouple (Omega), as described previously. There are no significant radial temperature gradients in the cylindrical tube, but the temperature does vary along the tube. A series of profiles was obtained at 100 °C intervals in

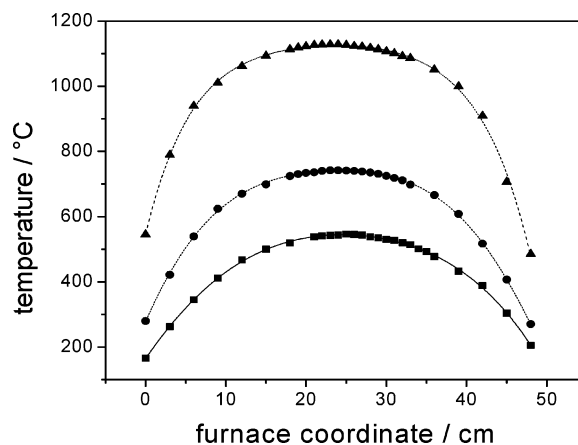


**Figure 2.** Temperature profiles as a function of distance in tube furnace for selected temperatures (data fit to 4th order polynomials): Set furnace temperature of 500 °C (■), set furnace temperature of 700 °C (●), set furnace temperature of 1100 °C (▲).

furnace setting, from 100 to 1100 °C. Several representative profiles are shown in Figure 2. The data points in each profile were fit to a 4th-order polynomial. Some oxidation measurements were made at furnace settings for which temperature profile measurements were unavailable. In such cases, profiles were estimated by linearly interpolating between two profiles for which profile measurements were available. The temperature profile measurements are considerably more extensive than those reported by us earlier.<sup>2</sup> The gas and particle temperatures were assumed to be equal. Previous work has shown this to be a valid assumption for soot particles of mobility diameter between 10 and 150 nm.<sup>28</sup>

The high-voltage supply for DMA-2 was remotely programmed using a PC with a multifunction board (National Instruments Lab-PC+) with a 12 bit D/A converter under software control. Scans were performed by incrementing the particle size by 1 nm, waiting 8 s for the flow to stabilize, and then collecting 5 readings from the UCPC at 2 s intervals. Chen and Kesten measured the size-dependent transmission efficiency of the nano-DMA model used for DMA-2, as well as the size-dependent counting efficiency of the UCPC.<sup>29,30</sup> Their measurements were used to correct the size distribution measurement.

For the TDMA scans, peaks in the corrected particle size distributions were fit to normal Gaussian functions using the Levenberg–Marquardt algorithm. The center of the Gaussian function was set as the particle size, and the area under the Gaussian was used as a surrogate for the total particle count. The algorithm also determined a 95% confidence interval for the mean; this interval was used to calculate the uncertainty of each data point. A single Gaussian was used to fit the data at low temperatures and oxygen pressures. At high temperatures (>1000 °C) and high oxygen pressures (>0.05 atm), multiple Gaussians had to be used to fit the size distributions, which were bimodal.

Transmission electron microscopy (TEM) images were obtained using a Tecnai T12 microscope. Particles were collected onto carbon film TEM grids immediately after mobility classification by DMA-1, using an electrostatic sampler biased at +3000 V.

## Results

Figure 3 shows two T-DMA scans, each corresponding to the oxidation of soot particles of original mobility diameter 40 nm at a peak furnace temperature of 1030 °C. In one experiment, the carrier gas was dry, filtered air (which contains ~20.9%

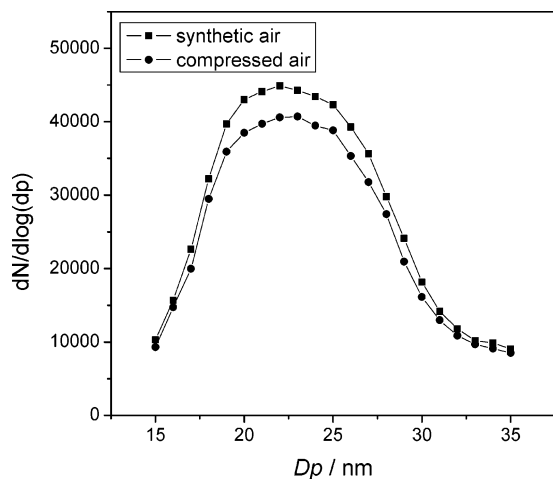


**Figure 3.** TDMA scans of the oxidation of 40 nm soot particles at 1000 °C with synthetic air  $\sim 79.1\%$   $N_2/20.9\%$   $O_2$  mixture (■) and compressed air,  $\sim 20.8\%$   $O_2$  (●).

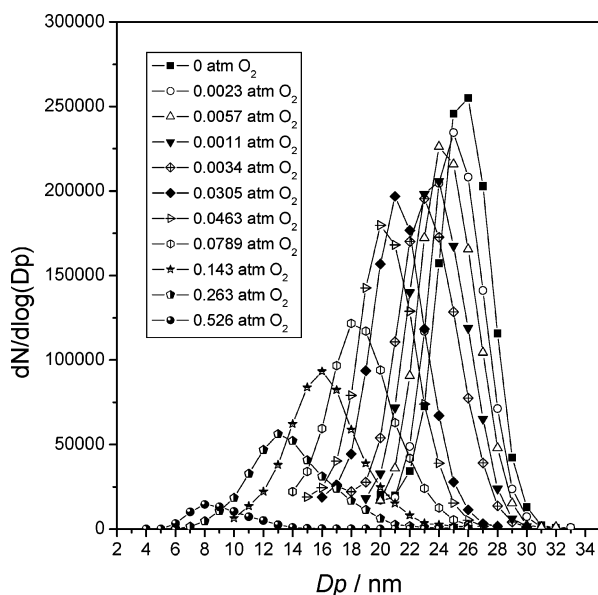


**Figure 4.** Representative TDMA data for the oxidation of 30 nm soot particles at 975 °C with  $N_2$ - $O_2$  mixtures with oxygen partial pressures from 0 to 0.526 atm. Some TDMA scans have been omitted for clarity.

oxygen by volume<sup>31</sup>); in the other experiment, the carrier gas was “synthetic air”, a mixture of  $N_2$  and  $O_2$  containing 20.8%  $O_2$  by volume. There are no significant differences between the two T-DMA scans. In particular, passage through the furnace results in the same reduction of peak mobility diameter, from 40.0 to 22.0 nm. The difference in peak heights of the two T-DMA scans is probably associated with the slightly different flow conditions in the two sets of experiments. We conclude (i) that a minority component of air is not responsible for the measured size reduction and (ii) that we are able to produce  $N_2/O_2$  mixtures of desired composition.

Reactions of soot nanoparticles with  $O_2$  were investigated over broad ranges of temperature and  $O_2$  volume fraction. Figure 4 shows a representative set of T-DMA scans for the oxidation of 30 nm initial mobility diameter particles at a peak furnace temperature of 975 °C. In this set of experiments, 23 scans were obtained, in which  $F_{O_2}$  was varied between 0 and 1. In the interest of clarity, several scans are omitted from Figure 4. From inspection of the data, it is clear that the particles decrease in size as they pass through the furnace and that the amount of size reduction increases with  $F_{O_2}$ . As will be shown below, the

**TABLE 1:**  $\Delta D_p^{N_2}$

set oven temperature/°C	$\Delta D_p^{N_2}/nm$
500	0.552
800	1.527
850	1.945
875	2.193
900	2.382
925	2.763
950	3.499
975	4.264
1000	5.075
1025	5.076
1050	5.569
1075	6.382
1100	6.857

decrease in peak mobility diameter ( $\Delta D_p$ ) can be related to the kinetics of the reaction between soot and molecular oxygen. From Figure 4, it is also apparent that the scan peak heights decrease with increasing oxygen volume fraction. Partly, this is because the size distributions broaden. However, the integrated peak areas of the scans decrease significantly as the extent of reaction increases, particularly for  $F_{O_2} > 0.05$ . Possible reasons for this behavior will be considered in the Discussion.

Some size reduction occurs even in pure nitrogen gas, when no oxidation is possible. For instance, for a furnace setting of 975 °C, the decrease in peak mobility diameter in pure nitrogen,  $\Delta D_p^{N_2}$ , is 4.3 nm. If it is assumed the nonoxidative and oxidative size reduction components are additive (as is justified below), then  $\Delta D_p^{O_2}$ , the size reduction resulting from oxidation, can be obtained from the equation

$$\Delta D_p^{O_2} = \Delta D_p - \Delta D_p^{N_2} \quad (2)$$

For the T-DMA scans obtained at a furnace setting of 975 °C,  $\Delta D_p^{O_2}$  ranges between  $-0.60$  nm at  $F_{O_2} = 0.0023$  (the most dilute  $O_2 + N_2$  mixture studied at this furnace setting) and  $-18.0$  nm for  $F_{O_2} = 0.53$ .

Size reduction data were obtained for 30 nm initial mobility diameter particles as a function of  $F_{O_2}$  at 13 furnace settings between 500 and 1100 °C. Scans that were obtained in pure nitrogen gas were used to determine  $\Delta D_p^{N_2}$  at each furnace setting; results are tabulated in Table 1. The measured values of  $\Delta D_p$  and  $\Delta D_p^{N_2}$  were then used to determine  $\Delta D_p^{O_2}$  for each T-DMA scan. The  $\Delta D_p^{O_2}$  measurements are summarized in Figure 5, in which  $\Delta D_p^{O_2}$  is plotted against  $F_{O_2}$  for each furnace setting. From these plots, two things are clear: first, that  $\Delta D_p^{O_2}$  increases with temperature at a fixed value of  $F_{O_2}$ , and, second, that  $\Delta D_p^{O_2}$  increases with  $F_{O_2}$  at constant temperature. The  $F_{O_2}$ -dependent data are particularly revealing in that they imply two different kinetic regimes for particle oxidation. At low oxygen partial pressures (up to  $F_{O_2}$  values of approximately 0.01), there is a “fast” oxidation regime in which  $\Delta D_p^{O_2}$  increases rapidly and linearly with  $F_{O_2}$ . Above  $F_{O_2} = 0.01$ , the reaction enters a “slow” regime, in which  $\Delta D_p^{O_2}$  continues to increase with  $F_{O_2}$ , but much more slowly than before. Possible reasons for this behavior will be discussed below.

Figure 6 shows a representative TEM image of soot particles collected immediately after exiting DMA-1, with the DMA set to pass particles of  $D_p = 30$  nm. Most of the particles are nearly spherical and of diameter  $\sim 30$  nm, as expected. Some of the particles are larger, with a diameter of  $\sim 60$  nm. These are attributed to particles that were doubly charged when they left DMA-1. When a statistically significant number of images are analyzed, the relative numbers of  $\sim 30$  and  $\sim 60$  nm particles

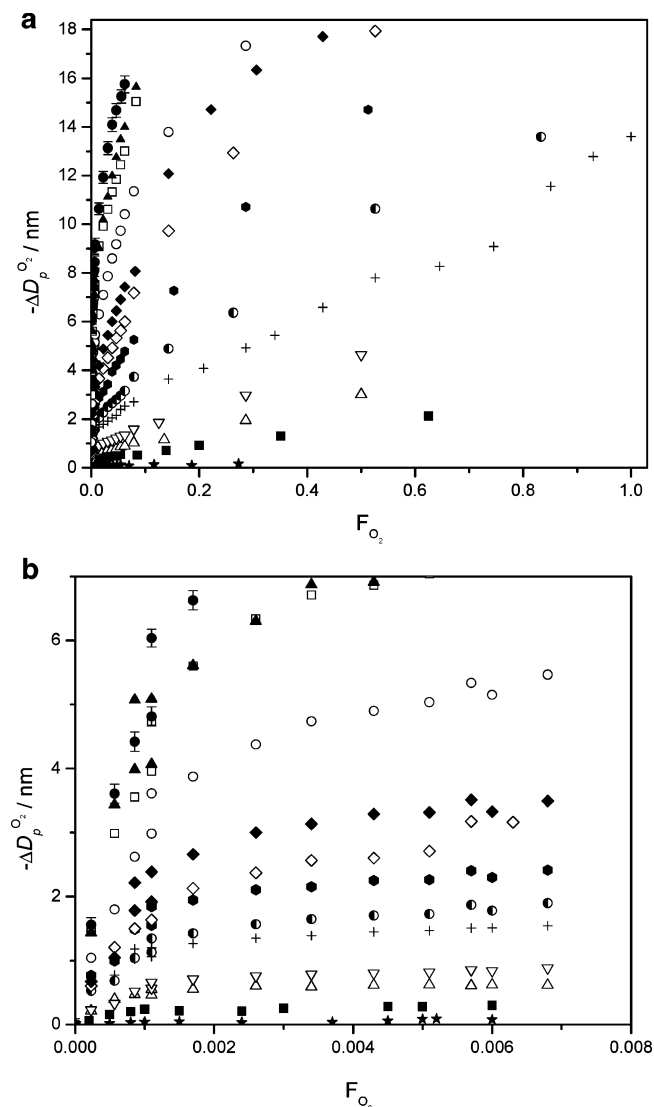


**Figure 5.** (a) Experimental particle size change as a function of  $F_{O_2}$  measured at peak furnace settings between 500 and 1100 °C. (b) The same data plotted between  $F_{O_2} = 0$  and 0.008, to better illustrate the break between the two oxidation rates. 500 °C (★), 800 °C (■), 850 °C (△), 875 °C (▽), 900 °C (+), 925 °C (half black circle), 950 °C (●), 975 °C (◇), 1000 °C (◆), 1025 °C (○), 1050 °C (□), 1075 °C (▲), and 1100 °C (●). Both figures display error bars for the 1100 °C data. Error bars for the other sets of data are omitted for clarity, but are of the same relative error.

are approximately what would be expected for particles that were ionized by a bipolar diffusion charger.

## Discussion

The T-DMA measurements establish that soot nanoparticles decrease in size as they pass through a high temperature furnace and that the amount of size reduction depends on temperature and gas-phase composition. In any given experiment, particles do not all shrink by the same amount, and the size distribution function of a particle stream therefore broadens as it passes through the furnace (see, for example, Figure 4). This broadening is probably associated mostly with the fact that gas flow is laminar or near-laminar, and as a result, particles experience a range of residence times in the reactor. No attempt was made to model how the shapes and widths of the distribution functions evolved with furnace setting. Instead, results were analyzed entirely in terms of  $\Delta D_p / \Delta t$ , where  $\Delta D_p$  is the change in peak

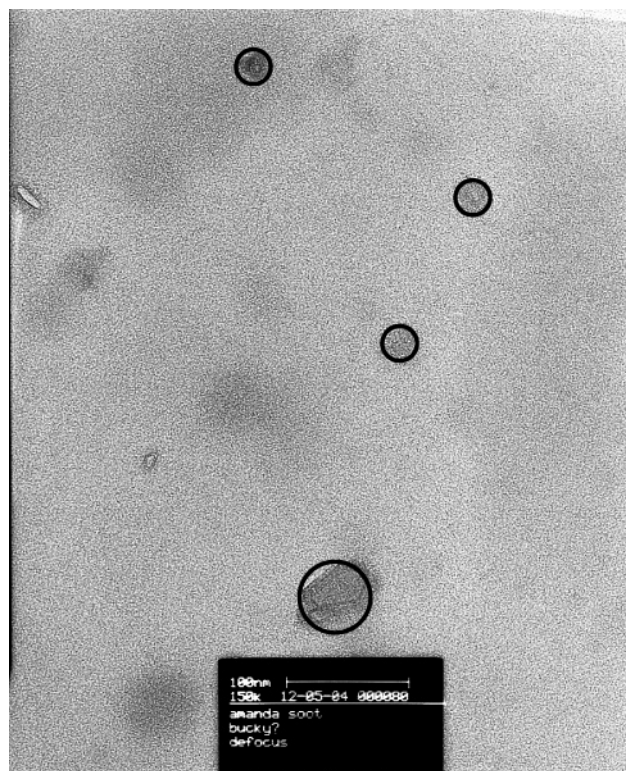


**Figure 6.** TEM image of soot nanoparticles collected on an electrostatic probe. The small circles enclose the images of roughly spherical particles having diameters of 30 nm. The larger circle encloses the image of a 60 nm particle, which passed through the DMA because it had two elementary charges.

mobility diameter and  $\Delta t$  is the characteristic residence time in the reactor, as inferred from the peak gas flow velocities.

The series of T-DMA scans shown in Figure 4 implies that the number of particles transported to the UCPC decreases as  $F_{O_2}$  increases. The origin of this behavior is unclear. The decreased particle numbers are not associated with some effect having to do with mixing ever larger amounts of  $O_2$  into the carrier gas, because an analogous series of scans recorded at a furnace setting of 500 °C shows no significant decrease in the number of particles detected by the UCPC. The most likely explanation for decreased particle numbers is wall loss. Because the diffusion rate of a particle increases as its size decreases, wall losses are more significant for small particles and, therefore, for particles that have undergone more extensive oxidation. As a test of this hypothesis, we plotted the fractional penetration of the particle streams against the calculated particle diffusion constant. Except for the highest and lowest temperature measurements, all data sets collapse onto the same curve. This implies that diffusional wall losses are an important reason for the decreasing particle numbers.

Particles undergo modest size reduction even when pure nitrogen is the carrier gas, as shown in Table 1. The size changes that occur in pure nitrogen are presumably not the result of material lost to the gas phase through chemical reactions, but instead are associated with physical processing. In earlier work on larger soot particles, we attributed nonoxidative shrinkage either to the evaporation of semivolatile material or to thermally induced restructuring of aggregates to more dense structures. The latter explanation seems less likely for the work reported here, because 30 nm mobility diameter particles are, on average, nearly spherical (Figure 6).<sup>32</sup> It is conceivable that primary soot particles are porous and subject to densification upon heating,

but a more plausible explanation is that heating in nitrogen results in the loss of semivolatile material.

For most of the measurements reported in this work,  $\Delta D_p$  is dominated by size changes that are associated with the presence of oxygen in the carrier gas. Molecular oxygen reacts with soot to produce gas-phase products, principally CO, one result of which is smaller soot particles. The question becomes, how to separate the oxidative and nonoxidative components of size reduction. Let us assume that size reduction results from two parallel processes, evaporation/densification and oxidation. At any given temperature and value of  $F_{O_2}$ , each process is described by an areal mass loss rate,  $\bar{R}_{N_2}$  for evaporation/densification and  $\bar{R}_{O_2}$  for oxidation, expressed in units of  $\text{g cm}^{-2} \text{s}^{-1}$ . The rate of mass loss in a single soot particle is then given by

$$-\frac{dm}{dt} = (\bar{R}_{N_2} + \bar{R}_{O_2})\sigma \quad (3)$$

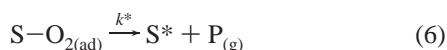
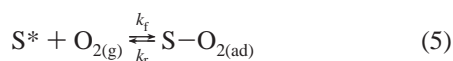
where  $\sigma$  is the particle surface area. For spherical particles in the molecular flow regime, the mobility diameter,  $D_p$ , of a particle may be taken as equal to its physical diameter, and eq 3 reduces to

$$\frac{dD_p}{dt} = -\frac{2}{\rho}(\bar{R}_{N_2} + \bar{R}_{O_2}) \quad (4)$$

where  $\rho$  is the density of soot. The implication is that, at any given temperature and value of  $F_{O_2}$ , the oxidative and non-oxidative components of  $\Delta D_p$  are additive, i.e., that eq 2 holds.

Plots of  $\Delta D_p^{O_2}$  versus  $F_{O_2}$  are not linear between  $F_{O_2} = 0$  and 1 (Figure 5), in contrast to what would be expected for a process that is first-order in oxygen partial pressure. Rather, there are two kinetic regimes, a “fast” regime in which  $\Delta D_p^{O_2}$  increases relatively rapidly with  $F_{O_2}$  and a “slow” regime in which  $\Delta D_p^{O_2}$  increases more slowly. One possible explanation for this behavior is that the particles have shell-like structures, consisting of refractory, graphitic cores surrounded by more readily oxidized shells. However, were that the case, the turnover from “fast” to “slow” kinetics would occur at the same  $\Delta D_p^{O_2}$  value, regardless of furnace setting, whereas the turnover occurs at approximately the same value of  $F_{O_2}$ . A “fluffy shell” model cannot explain the experimental observations.

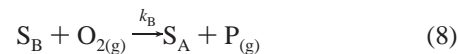
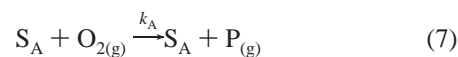
A second possibility is that oxidation occurs via a Langmuir–Hinshelwood or related mechanism. Under Langmuir–Hinshelwood kinetics, oxidation would proceed via the formation of a surface–oxygen complex followed by the decomposition of that complex



where  $S^*$  is a reactive surface site,  $S-O_{2(ad)}$  is the surface–oxygen complex,  $k_f$  and  $k_r$  are the forward and reverse rate constants, respectively, for formation of the complex,  $k^*$  is the rate constant for decomposition of the complex, and  $P_{(g)}$  represents the primary gas-phase products (almost certainly CO). A Langmuir–Hinshelwood model predicts two kinetic regimes. At low oxygen pressures, gas-phase product formation is limited by  $S-O_{2(ad)}$  formation, and the rate is therefore controlled by gas–surface collisions. At high enough pressures, however, the surface becomes saturated with adsorbed oxygen. The reaction rate is limited by the rate of  $S-O_{2(ad)}$  decomposition and

therefore independent of oxygen pressure. There is no single solution to the Langmuir–Hinshelwood model; the solution depends, for instance, on the orders of the elementary reaction steps with respect to oxygen pressure and surface site coverage. However, for any physically reasonable kinetic description of eqs 5 and 6, surface saturation effects would eventually cause the reaction rate to become independent of oxygen pressure, with a relatively rapid transition from pressure-dependent to pressure-independent kinetics. The data reported in this work show no signs of any such plateau, even as the gas composition approaches pure oxygen. A Langmuir–Hinshelwood model seems unlikely.

A model that successfully explains how the soot oxidation rate depends on temperature and oxygen volume fraction is one that invokes two kinetically distinguishable surface oxidation sites,  $S_A$  and  $S_B$ . The model is a variant of ones suggested by Blyholder, Binford, and Eyring<sup>5</sup> and Nagle and Strickland-Constable.<sup>6,8</sup> In our two site model,  $S_A$  and  $S_B$  react with molecular oxygen to generate gas-phase products. Each of these reactions is first order in oxygen pressure and first order in vacant site coverage. The two sites are characterized by different modified Arrhenius rate constants ( $k_A$  and  $k_B$ ), but equally important, they differ in that reaction at  $S_A$  regenerates  $S_A$ , whereas reaction at  $S_B$  results in formation of a new A site



For completeness sake, and to guarantee that steady-state conditions are met, the model also allows for thermally activated interconversion between A and B



We now solve for the oxidation rate in terms of the experimentally measurable quantities,  $\Delta D_p^{O_2}$ ,  $T$ , and  $F_{O_2}$ . From eqs 3 and 4, it follows that  $dD_p^{O_2}/dt$ , the rate of change of mobility diameter due to oxidation, is

$$\frac{dD_p^{O_2}}{dt} = -\frac{2}{\rho}\bar{R}_{O_2} \quad (10)$$

where  $\bar{R}_{O_2}$ , the rate of oxidative mass loss per unit surface, is the sum of the rates on sites A and B. If oxidation at both sites A and B is first order in oxygen pressure and site coverage, then

$$\bar{R}_{O_2} = k_A Z_{O_2} (M_C/N_A) \theta_A + k_B Z_{O_2} (M_C/N_A) \theta_B \quad (11)$$

where  $\theta_A$  and  $\theta_B$  are the fractional coverages of sites A and B, respectively,  $Z_{O_2}$  is the collision rate between  $O_2$  and the surface expressed in units of  $\text{cm}^{-2} \text{s}^{-1}$ ,  $M_C$  is the formula mass of soot, which we take as equal to the molar mass of elemental carbon, and  $N_A$  is Avogadro’s number. Because A and B are interconvertible, it is reasonable to assume that the total number of A and B sites per unit surface area is fixed at  $\theta^*$ . In that case, eq 11 reduces to

$$\bar{R}_{O_2} = \frac{Z_{O_2} M_C}{N_A} [(k_A - k_B) \theta_A + k_B \theta^*] \quad (12)$$

As long as the reaction rate parameters are independent of

particle size,  $\bar{R}_{O_2}$ ,  $\theta_A$ , and  $\theta_B$  will reach steady-state values under conditions of fixed temperature and oxygen pressure. If we assume that the reactions which thermally interconvert A and B (i.e., the forward and reverse of eq 9) are first-order in site coverage, then  $\theta_A^{ss}$ , the steady-state fractional coverage of A, may be calculated by considering the competition between A formation (eq 8 and the reverse of eq 9) and destruction (the forward of eq 9)

$$k_B(Z_{O_2}/N^*)(\theta^* - \theta_A^{ss}) - k_{A \rightarrow B}\theta_A^{ss} + k_{B \rightarrow A}(\theta^* - \theta_A^{ss}) = 0 \quad (13)$$

where  $N^*$  is the density of atoms at the soot surface in units of  $\text{cm}^{-2}$ . Substituting into eq 10, and assuming that the reactions reach steady-state very quickly, we obtain

$$\frac{dD_p^{O_2}}{dt} = -\frac{2Z_{O_2}M_C\theta^*}{N_A\rho} \left\{ \frac{[(k_B Z_{O_2}/N^*) + k_{B \rightarrow A}]k_A + k_{A \rightarrow B}k_B}{(k_B Z_{O_2}/N^*) + k_{A \rightarrow B} + k_{B \rightarrow A}} \right\} \quad (14)$$

Qualitatively, eq 14 explains the experimentally observed trends. In particular, it predicts two kinetic regimes, at low and high oxygen partial pressures. In both regimes, the size reduction rate is expected to depend linearly on oxygen partial pressure

$$\text{low pressure limit: } \frac{dD_p^{O_2}}{dt} = -\frac{2 \cdot Z_{O_2} \cdot M_C \cdot \theta^*}{N_A \cdot \rho} \cdot \left( \frac{k_{B \rightarrow A} \cdot k_A + k_{A \rightarrow B} \cdot k_B}{k_{A \rightarrow B} + k_{B \rightarrow A}} \right) \quad (15)$$

$$\text{high pressure limit: } \frac{dD_p^{O_2}}{dt} = -\frac{2 \cdot Z_{O_2} \cdot M_C \cdot \theta^*}{N_A \cdot \rho} \cdot k_A \quad (16)$$

This qualitative agreement is gratifying, but in the following paragraphs we demonstrate that eq 14 can be quantitatively fit to the  $\Delta D_p^{O_2}$  measurements. Remarkably, excellent agreement between experiment and the model is obtained using a single set of eight Arrhenius parameters, two for each of the elementary steps described by eqs 7–9, to predict size reduction for all of the 13 furnace settings studied.

Before eq 16 can be used for quantitative data interpretation, we must identify the functional forms of the rate constants and assign values to certain constants. All rate constants,  $k_i$ , are assumed to be adequately described by a modified Arrhenius expression

$$k_i = A_i T^{1/2} e^{-E_i/RT} \quad (17)$$

where  $A_i$  and  $E_i$  are the reaction prefactors and activation energies, respectively. The collision rate of oxygen with the surface may be calculated from gas kinetic theory, taking the oxygen partial pressure, in units of atm, as numerically equal to  $F_{O_2}$ . The density of a particle,  $\rho$ , is taken as equal to the density of bulk soot, or  $1.80 \text{ g cm}^{-3}$ . The surface site density,  $N^*$ , is assigned the value  $2.01 \times 10^{15} \text{ cm}^{-2}$ , which corresponds to the density of exposed atoms in a hypothetical cubic carbon lattice of  $\rho = 1.80 \text{ g cm}^{-3}$ . As can be inferred from eqs 15–16, an error in the value chosen for  $\rho$  or  $N^*$  will result in a corresponding error of the fitted values of the prefactors but not of the activation energies.

Equation 14 describes the particle oxidation rate at a single temperature, but the particle streams experience nonuniform temperature fields in the furnace. Moreover, gas expansion

effects cause the gas flow velocities to vary with furnace position. In a laminar flow system of constant cross-sectional area, the position-dependent peak flow velocity,  $u(x)$ , is described by the equation

$$u(x) = \frac{4}{3} \frac{T(x)}{T_0} u_0 \quad (18)$$

where  $T(x)$  is the temperature at  $x$ , and  $T_0$  and  $u_0$  are the temperature and mean flow velocity measured at some other position in the reactor. If a furnace of length  $L$  is assigned the coordinate  $x = 0$  at its entrance, then the total oxidative size reduction is given by

$$\Delta D_p^{O_2} = \int_0^L \left( \frac{dD_p^{O_2}}{dt} \right) \left( \frac{1}{u(x)} \right) dx \quad (19)$$

We now have an equation which can be used to predict total oxidative size reduction as functions of  $F_{O_2}$  and furnace setting.

Equation 19 was fit to the  $\Delta D_p^{O_2}$  measurements using a microgenetic algorithm. Genetic algorithms were first developed in the late 1960s to model biological reproduction,<sup>33</sup> but they have developed into a method for iteratively fitting complex, nonlinear data sets. Details of genetic algorithms and their applications are described elsewhere. In brief, an initial population of “chromosomes” is defined, which for the present application was an array of sets of Arrhenius parameters. A cost function, defined so that the “best” chromosomes have the lowest cost, is evaluated for each chromosome in the population. The best chromosomes of the new population are allowed to mate and mutate to form a next generation. A new cost function is evaluated, and the mating/mutation/cost evaluation process is repeated until convergence is achieved.<sup>34,35</sup>

In this work, a microgenetic algorithm was employed to fit the data, with single-point crossover, tournament selection, and an initial population of 20 chromosomes. Each chromosome was a set of eight Arrhenius parameters, two for each of the elementary steps shown in eqs 7–9. The values of  $A_A$  and  $A_B$  were constrained so that  $k_A$  and  $k_B$  were always less than unity, so as to exclude nonphysical solutions. Other Arrhenius parameters were unconstrained. The cost function,  $f$ , was defined as the sum over all data points of the absolute value of the percent difference between the model prediction for  $\Delta D_p^{O_2}$  ( $\Delta D_p^{O_2, \text{calc}}$ ) and its corresponding experimental measurement ( $\Delta D_p^{O_2, \text{meas}}$ )

$$f = \sum \left| \frac{\Delta D_p^{O_2, \text{meas}} - \Delta D_p^{O_2, \text{calc}}}{\Delta D_p^{O_2, \text{calc}}} \right| \times 100 \quad (20)$$

Evaluation of  $\Delta D_p^{O_2, \text{calc}}$  required that eq 19 be numerically integrated. The furnace was divided into 451 hypothetical finite elements of equal length, with the temperature of each element assigned by reference to the temperature profiles described in the Experimental Section.

The Arrhenius parameters that come out of the fitting procedure are shown in Table 2. The activation energies of the two oxidation steps are  $151 \text{ kJ mol}^{-1}$  for reaction at  $S_A$  and  $98 \text{ kJ mol}^{-1}$  for oxidation at  $S_B$ . The higher activation energy value is associated with the process that dominates at high  $F_{O_2}$ . Previous measurements of soot oxidation in air, which would correspond to the high pressure regime, have generally reported activation energies between  $140$  and  $170 \text{ kJ mol}^{-1}$ .<sup>5</sup> Interestingly,  $A_A$  and  $A_B$ , the oxidation prefactors, are within 10% of each other ( $0.750$  and  $0.705 \text{ K}^{-1/2}$ , respectively). The prefactors

**TABLE 2: Kinetic Parameters**

$S_A + O_2 \rightarrow S_A + 2CO$	
$A_A$	$0.750 \text{ K}^{-1/2}$
$E_{A_A}$	$151 \text{ kJ mol}^{-1}$
$S_B + O_2 \rightarrow S_A + 2CO$	
$A_A$	$0.705 \text{ K}^{-1/2}$
$E_{A_A}$	$98.0 \text{ kJ mol}^{-1}$
$S_A \rightarrow S_B$	
$A_{A \rightarrow B}$	$6.71 \times 10^6 \text{ K}^{-1/2} \text{ s}^{-1}$
$E_{A \rightarrow B}$	$135.56 \text{ kJ mol}^{-1}$
$S_B \rightarrow S_A$	
$A_{B \rightarrow A}$	$5.65 \times 10^9 \text{ K}^{-1/2} \text{ s}^{-1}$
$E_{B \rightarrow A}$	$489 \text{ kJ mol}^{-1}$

are also quite close to their constrained maximum values. The activation energies for site interconversion indicate that these reactions are quite slow. Indeed the quality of the fit is only weakly dependent on the Arrhenius parameters for site interconversion. Figure 7 plots  $\Delta D_p^{O_2, \text{meas}}$  and  $\Delta D_p^{O_2, \text{calc}}$  versus  $F_{O_2}$  for several representative furnace settings (800, 900, and 1025 °C). Agreement between experiment and the model is remarkable, especially considering that only eight parameters were used to fit data obtained over wide ranges of temperature and oxygen partial pressure. The mean percent difference between  $\Delta D_p^{O_2, \text{meas}}$  and  $\Delta D_p^{O_2, \text{calc}}$  for all data sets was 22%; for furnace settings of 900 °C or greater (where the reaction rates were higher and the measurements correspondingly less uncertain), the mean difference was 12%. Just as significant, the model predicts the value of  $F_{O_2}$  at which the reaction “turns over” from the rapid to the slow oxidation regime.

The most widely cited kinetic model for soot oxidation is that of Nagle and Strickland-Constable (NSC). NSC was originally developed as a method for predicting oxidation rates at relatively high temperatures (1000–2400 °C) and atmospheric pressure. However, because NSC is reasonably successful even at temperatures below 1000 °C, and because it explicitly considers the oxygen partial pressure dependence, it is a necessary starting point in any discussion of a new or refined kinetic model. NSC is conceptually similar to the model developed in this work. In particular, the two models postulate two oxidation sites, A and B, which undergo rapid thermal interconversion, as in eq 9. In both cases, B is also converted back to A through oxidation. For both NSC and the model described herein, good fits to the experimental data require an activation energy for A oxidation in the vicinity of 150 kcal mol<sup>-1</sup>. Where the models disagree is in fitted values of the activation energy for B oxidation: NSC finds that  $E_B > E_A$ , whereas we conclude the opposite. This disagreement is of some concern, and we cannot offer an explanation except to point out that the models, although similar, were developed to rationalize different observations. In particular, in the case of NSC, the two sites are invoked to explain temperature-dependent measurements which show that oxidation rates decrease with increasing temperature above  $\sim 1900$  °C. In NSC, the reaction slows down at high temperatures because the site interconversion equilibrium heavily favors  $S_B$  above 1900 °C, and this site reacts more slowly with oxygen.

In Figure 8, we compare our measurements of the pressure-dependent oxidation rate at 1100 °C with the predictions of the two kinetic models. As would be expected, the model described here, which was developed specifically to rationalize the pressure dependent measurements, agrees better with the data

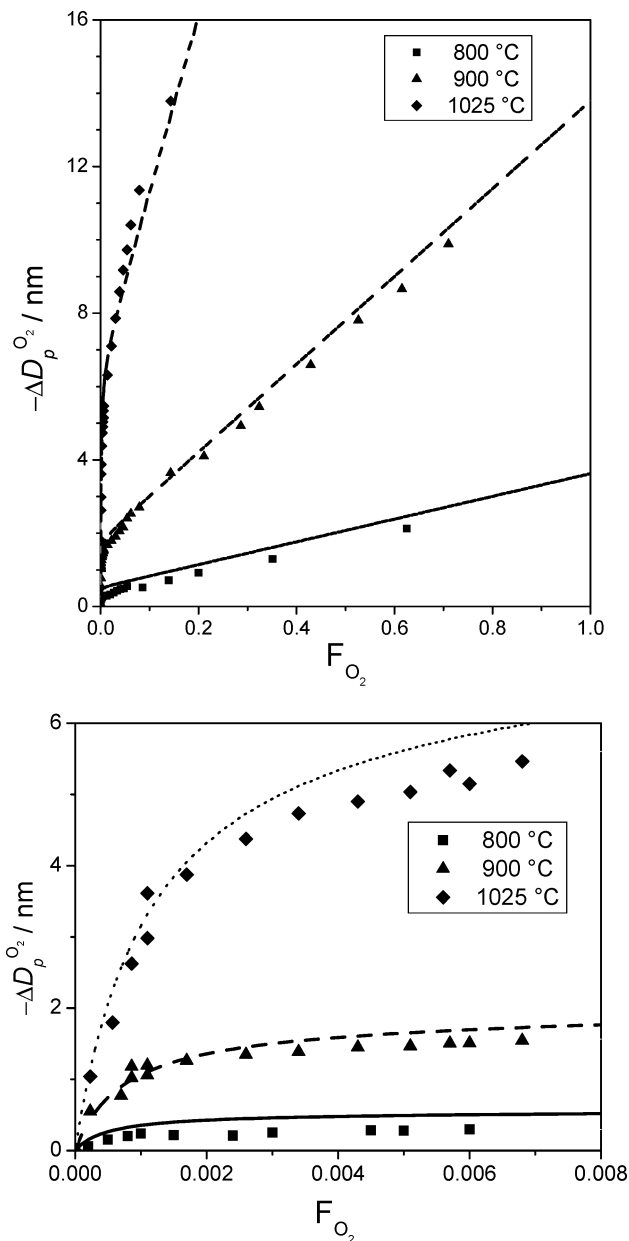


**Figure 7.** (a) Particle size change as a function of oxygen concentration at 800 °C (■), 900 °C (▲), and 1025 °C (◆). Solid lines show size change calculated from the fitted model. (a) The same data plotted between  $F_{O_2} = 0$  and 0.008, to better illustrate the break between the two oxidation rates.

than does NSC. In particular, although NSC does predict low and high partial pressure regimes for oxidation, the high pressure regime is nearly independent of oxygen partial pressure, implying a mass transport-limited process. The two models are close in their rate predictions at an oxygen partial pressure of 0.2 atm (i.e., in air), which is consistent with the fact that the data sets both models attempt to model include measurements at 0.2 atm.

The literature on soot oxidation encompasses literally hundreds of experimental studies on soot and soot surrogates. Although most of these studies concern oxidation in air at atmospheric pressure and are therefore of limited relevance to this work, some pressure dependent work has been reported. Figure 8 compares our measurements of the pressure-dependent oxidation rate at 1100 °C to those published in several of these studies. Where necessary, the measurements from other studies are extrapolations to 1100 °C using the rate expressions

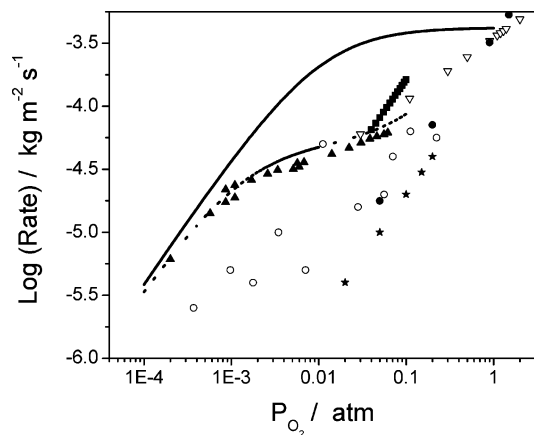


**Figure 8.** Comparison of the current data with published oxidation data at 1100 °C. (▲) Represents the current experimental work with 30 nm particles at 1100 °C; (---) represents the proposed model. A density of 1800 kg/m<sup>3</sup> was assumed. The activation energy, rates, and surface areas from Park and Appleton (●, ref 16), Otto, et al. (★, ref 22), and Cadman and Denning (▽, ref 24) were used to extrapolate their data to a temperature of 1100 °C. Data from Lee, Thring, and Beer (■, ref 23) and Felder, Madronich, and Olson (○, ref 15) were taken directly from the papers. (—) demonstrates the Nagle and Strickland-Constable model (ref 8).

published in those studies. In general, there is reasonable agreement between the different measurements, especially considering the wide range of samples and methods employed. None of these studies identify a rapid oxidation regime at low partial pressures. However, almost all of the studies considered oxygen partial pressures for which reaction would be dominated by the slow oxidation regime. A notable exception is a paper by Otto et al., which describes the oxidation of diesel soot deposits at 350 °C and oxygen partial pressures between 0.04 and 0.25 atm. A single oxidation regime was identified, which was first order in oxygen partial pressure. When these measurements are extrapolated to 1100 °C, the prediction is of a single first-order regime, with rates that are uniformly higher than those we measured. However, we do not view this as a serious disagreement: diesel soot is potentially different from ethene soot, an extrapolation from 350 to 1100 °C is problematic, and Otto et al.'s data show considerable scatter.

**Acknowledgment.** The authors thank Nathan E. Schultz for help developing the genetic algorithm and Ryan S. Thompson for aid with the TEM imaging. This material is based on work supported by the National Science Foundation under Grant No. 0094911. A.M.N. acknowledges partial support by the Integrative Graduate Education and Research Traineeship (IGERT) in Nanoparticle Science and Engineering at the University of Minnesota, which is funded by the National Science Foundation under Grant No. 0114372.

## References and Notes

- (1) Hinds, W. C. *Aerosol Technology: Properties, Behavior and Measurement of Airborne Particles*, 2 ed.; John Wiley and Sons: New York, 1999.
- (2) Higgins, K. J.; Jung, H.; Kittelson, D. B.; Roberts, J. T.; Zachariah, M. R. *J. Phys. Chem.* **2002**, *106*, 96–103.
- (3) Seinfeld, J. H.; Pandis, S. N. *Atmospheric Chemistry and Physics: From Air Pollution to Climate Change*; John Wiley and Sons: New York, 1998.
- (4) Gilot, P.; Bonnefoy, F.; Marcuccilli, F.; Prado, G. *Combust. Flame* **1993**, *95*, 87–100.
- (5) Stanmore, B. R.; Brilhac, J. F.; Gilot, P. *Carbon* **2001**, *39*, 2247–2268.
- (6) Blyholder, G.; Binford, J. S.; Eyring, H. *J. Phys. Chem.* **1958**, *62*, 263–267.
- (7) Strickland-Constable, R. F. *Trans. Faraday Soc.* **1944**, *40*, (333–343).
- (8) Nagle, J.; Strickland-Constable, R. F. In *5th Carbon Conference*; Pergamon: Oxford, 1962; Vol. 1, pp 154–164.
- (9) Walls, J. R.; Strickland-Constable, R. F. *Carbon* **1964**, *1*, 333–338.
- (10) Ranish, J. M.; Walker, P. L. *Carbon* **1993**, *31* (1), 135–141.
- (11) Yang, R. T.; Wong, C. *J. Chem. Phys.* **1981**, *75* (9), 4471–4476.
- (12) Kelemen, S. R.; Freund, H. *Carbon* **1985**, *23* (6), 619–625.
- (13) Starsinic, M.; Taylor, R. L.; Walker, P. L.; Painter, P. C. *Carbon* **1983**, *21* (1), 69–74.
- (14) Ciambelli, P.; D'Amore, M.; Palma, V.; Vaccaro, S. *Combust. Flame* **1994**, *99*, 413–421.
- (15) Felder, W.; Madronich, S.; Olson, D. B. *Energy Fuels* **1988**, *2*, 743–750.
- (16) Park, C.; Appleton, J. P. *Combust. Flame* **1973**, *20*, 369–379.
- (17) Du, Z.; Sarofim, A. F.; Longwell, J. P.; Mims, C. A. *Energy Fuels* **1991**, *5*, 214–221.
- (18) Neeft, J. P. A.; Nijhuis, T. X.; Smakman, E.; Makkee, M.; Moulijn, J. a. *Fuel* **1997**, *76* (12), 1129–1136.
- (19) Schafer, T.; Maus, F.; Bockhorn, H.; Fetting, F. *Z. Naturforsch., A: Phys. Sci.* **1995**, *50*, 1009–1022.
- (20) Garo, A.; Prado, G.; LaHaye, J. *Combust. Flame* **1990**, *79*, 226–233.
- (21) Feugier, A. *Combust. Flame* **1972**, *19*, 249–256.
- (22) Otto, K.; Sieg, M. H.; Zinbo, M.; Bartosiewicz, L. *SAE Technol. Pap. Ser* **1980**, No. 800336.
- (23) Lee, K. B.; Thring, M. W.; Beer, J. M. *Combust. Flame* **1962**, *6*, 137–145.
- (24) Cadman, P.; Denning, R. J. *J. Chem. Soc., Faraday Trans.* **1996**, *92* (21), 4159–4165.
- (25) Higgins, K. J.; Jung, H.; Kittelson, D. B.; Roberts, J. T.; Zachariah, M. R. *Environ. Sci. Technol.* **2003**, *37*, 1949–1954.
- (26) Wiedensohler, A. *J. Aerosol Sci.* **1988**, *19*, 387–389.
- (27) Fuchs, N. A. *Geophys. Pura Appl.* **1963**, *56*, 185–193.
- (28) Jung, H. *Size-Selected Nanoparticle Chemistry: Kinetics of Soot Oxidation*; University of Minnesota: Minneapolis, MN, 2003.
- (29) Kesten, J.; Reineking, A.; Porstendorfer, J. *Aerosol Sci. Technol.* **1991**, *15*, 107–111.
- (30) Chen, D.-R.; Pui, D. Y. H.; Hummes, D.; Fissan, H.; Quant, F. R.; Sem, G. J. *J. Aerosol Sci.* **1998**, *29* (5/6), 497–509.
- (31) Lide, D. R. *Handbook of Chemistry and Physics*, 76th ed.; CRC Press: Boca Raton, FL, 1995.
- (32) Clague, A. D. H.; Donnet, J. B.; Wang, T. K.; Peng, J. C. M. *Carbon* **1999**, *37*, 1553–1565.
- (33) Hibbert, D. B. *Chemom. Intell. Lab. Syst.* **1993**, *19*, 277–293.
- (34) Krishnakumar, K. *SPIE: Intell. Control Adaptive Syst.* **1989**, *1196*, 289–296.
- (35) Haupt, R. L.; Haupt, S. E. *Practical Genetic Algorithms*, ed.; John Wiley and Sons: New York, 1998.